

Simulation of malaria-infected red blood cells in microfluidic channels: Passage and blockage

Tenghu Wu¹ and James J. Feng^{1,2,a)}

¹Department of Chemical and Biological Engineering, University of British Columbia, Vancouver, British Columbia V6T 1Z3, Canada

²Department of Mathematics, University of British Columbia, Vancouver, British Columbia V6T 1Z2, Canada

(Received 29 May 2013; accepted 26 July 2013; published online 6 August 2013)

Malaria-infected red blood cells (iRBCs) become less deformable with the progression of infection and tend to occlude microcapillaries. This process has been investigated *in vitro* using microfluidic channels. The objective of this paper is to provide a quantitative basis for interpreting the experimental observations of iRBC occlusion of microfluidic channels. Using a particle-based model for the iRBC, we simulate the traverse of iRBCs through a converging microfluidic channel and explore the progressive loss of cell deformability due to three factors: the stiffening of the membrane, the reduction of the cell's surface-volume ratio, and the growing solid parasites inside the cell. When examined individually, each factor tends to hinder the passage of the iRBC and lengthen the transit time. Moreover, at sufficient magnitude, each may lead to obstruction of narrow microfluidic channels. We then integrate the three factors into a series of simulations that mimic the development of malaria infection through the ring, trophozoite, and schizont stages. These simulations successfully reproduce the experimental observation that with progression of infection, the iRBC transitions from passage to blockage in larger and larger channels. The numerical results suggest a scheme for quantifying iRBC rigidification through microfluidic measurements of the critical pressure required for passage. © 2013 AIP Publishing LLC. [<http://dx.doi.org/10.1063/1.4817959>]

I. INTRODUCTION

Healthy red blood cells (RBCs) have a biconcave shape with a diameter of 7–8 μm and a thickness of 2–3 μm .¹ During their normal function, RBCs traverse the circulatory system, squeezing through capillaries as small as 3 μm in diameter. Their high deformability is mainly due to their excess surface area and extremely flexible membrane. When infected by the malaria-causing parasite *Plasmodium falciparum*, however, the RBC gradually loses its deformability through the three stages of infection—ring, trophozoite, and schizont—as the parasite grows and multiplies asexually within the infected RBC (iRBC).^{2–4} A direct consequence of the hardening of the iRBC is occlusion of microcapillaries, which causes the most severe symptoms of malaria.⁵

The rigidification of iRBC has been quantified using several experimental protocols: micropipette aspiration,⁶ stretching by optical tweezers,^{7–9} and passage through microfluidic channels.^{10–12} Aspiration and stretching of RBCs directly test their deformation under mechanical forcing and have yielded considerable insight into the hardening of the cells. So far, three mechanisms have been identified for the loss of deformability of the iRBC. First, the iRBC membrane hardens as parasitogenic proteins induce abnormal cross-linking of the spectrin network.¹³ Second, transport of liquid and proteins across the compromised cell membrane alters the iRBC's surface-to-volume ratio and swells the cell.^{14,15} Finally, the solid parasites inside the iRBC,

^{a)}Author to whom correspondence should be addressed. Electronic mail: jfeng@chbe.ubc.ca

known as merozoites, mechanically hinder cell deformation, especially when they grow in size and multiply by mitosis in the schizont stage.^{6,9}

With the advent of microfluidic assaying, microfluidic channels have been increasingly used as a tool for probing the mechanical property of cells. For malaria-infected RBCs, microfluidics brings one great advantage: it mimics the geometry in microcapillaries and in the spleen,¹⁶ where the red cells are forced through narrow passages. Consequently, it may potentially bridge the gap between idealized mechanical measurements using micropipettes and optical tweezers and *in vivo* events of interest, such as occlusion of capillaries and filtering of hardened RBCs in the spleen.^{2,16,17} Several groups^{10–12,18–21} have employed microfluidic channels to probe the deformability of healthy and malaria-infected red cells. Typically, a prescribed pressure drop is applied to push iRBCs through microfluidic channels of various sizes. For example, Shelby *et al.*¹⁰ demonstrated that with progression of the infection, the iRBC hardens gradually and blocks larger and larger pores (Fig. 1). In the development of biomechanical assay, Ma and coworkers^{12,22,23} measured the critical pressure required to push a cell through a constriction, and extracted a cortical tension through the Young-Laplace equation. This serves as a general indicator of the cell's rigidity. So far, however, experimental work in this area has remained largely qualitative. It would be desirable to establish a *quantitative connection* between the geometric and mechanical attributes of iRBCs and their ability to traverse microchannels or blood vessels of a certain size.

Such a quantification typically requires a computer simulation,¹¹ and only a few have appeared in the literature in recent years. Quinn *et al.*²⁴ used dissipative particle dynamics to compute the passage of a healthy RBC through a microfluidic channel. Bow *et al.*¹¹ extended that work to ring-stage iRBCs. Aingaran *et al.*¹⁷ used finite elements to compute the critical pressure required to push gametocytes of *Plasmodium falciparum* through a splenic slit. Imai *et al.*²⁵ presented a simulation of an iRBC blocking the entry to a narrow microfluidic channel. These studies have illustrated the capability of several numerical methods for simulating the passage of RBCs through microfluidic channels. But none has systematically analyzed how the structural and mechanical changes due to malaria infection affect the dynamics of iRBC in microfluidic channels.

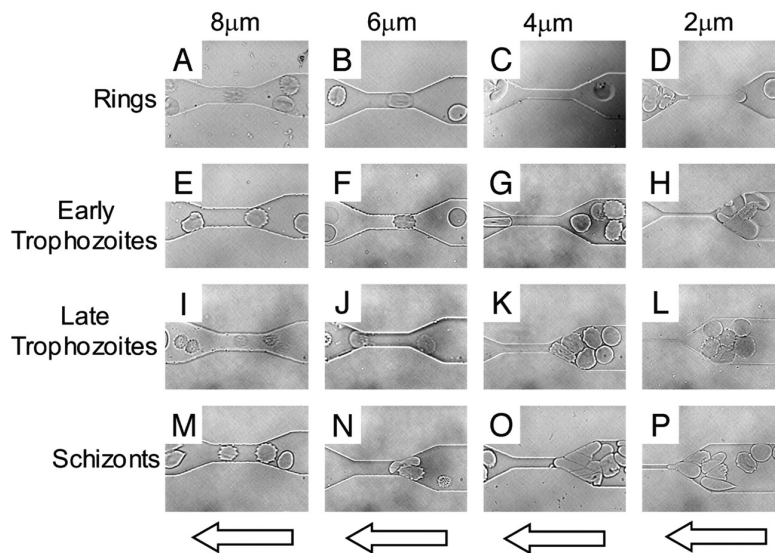


FIG. 1. Passage and blockage of microfluidic channels of different sizes by iRBC in the ring, trophozoite, and schizont stages of infection. The flow goes from the right to the left. Reprinted with permission from Shelby *et al.*, "A microfluidic model for single-cell capillary obstruction by *Plasmodium falciparum*-infected erythrocytes," Proc. Natl. Acad. Sci. U.S.A. **100**, 14618–14622 (2003). Copyright 2003 The National Academy of Sciences, U.S.A.

This paper aims to provide such a quantitative analysis through a systematic parametric study. By using a particle-based formalism in three dimensions (3D), we simulate the transit of healthy and infected RBCs through a prototypical microfluidic channel with a contraction. The surrounding fluid and the red cell, including the membrane, cytosol, and possibly the merozoite, are all discretized by particles in the framework of smoothed particle hydrodynamics (SPH).⁹ The interaction among the membrane particles is designed to produce an overall constitutive behavior similar to the commonly used hyperelastic models. By studying the transit time and critical condition for occlusion, we delineate the contribution to iRBC rigidification from each of the three mechanisms, hardening of the membrane, loss of excess surface area, and growth of the merozoite. The results not only shed light on *in vivo* RBC behavior in microcapillaries and in the spleen but also provides guidelines for designing sensitive microfluidic assays.

II. PHYSICAL MODEL AND NUMERICAL SCHEME

Most of the cell-mechanical simulations so far are based on continuum models, ranging from the liquid drop model to vesicle models.^{26–28} Particle-based models are relatively new, and by virtue of their meshless formalism, enjoy greater flexibility in representing morphological and structural changes in the cell or intracellular components.⁹ It is mostly this advantage that drew us to a particle-based model.

The physical model in this work is similar to that used by Hosseini and Feng⁹ and Imai *et al.*²⁵ We discretize the cytosol and surrounding plasma by particles much as in traditional SPH models for flow computation. The cell membrane is tessellated into more or less regular triangles, the vertices being represented by particles and the edges by springs. Thus, the membrane is discretized into a particle-spring network. The parasite is realized numerically by constraining a set of particles to move as a rigid body,²⁹ which floats in the cytosol. The motion of the “fluid particles,” representing the cytosol and plasma, is computed using the conventional SPH method and reproduces the fluid flow governed by the Navier-Stokes equations. The membrane particles experience bending and in-plane elasticity in addition to fluid pressure and viscous stress, as explained below.

The numerical solution is based on the open-source SPH solver parallelSPHysics,³⁰ developed for simulating fluid flows with free surfaces.^{31,32} On the basis of the original parallelized FORTRAN code, we have adopted an algorithm for floating solid objects to simulate the parasite and added the treatment of the cell membrane. The parallelization is realized through domain decomposition, and the interaction among particles that reside in different cores is realized by the MPI formalism.³⁰

A. Cell membrane elasticity

The cell membrane is represented by a discrete particle-spring network, which will be endowed with elasticity against in-plane strain and bending. We use linear springs with a stretching coefficient of k_s such that the elastic energy for in-plane deformation is

$$E_s = \sum_{ij} \frac{k_s}{2} (L_{ij} - L_{ij,0})^2, \quad (1)$$

where the summation is over all pairs of adjacent vertices i and j , L_{ij} is the length of the spring connecting them, and $L_{ij,0}$ is its resting length. For bending, Hosseini and Feng⁹ used the Helfrich bending energy³³ to compute the distribution of bending forces on the membrane particles. We found this formalism to be quite sensitive to the quality of the mesh; when the cell undergoes large deformation, the distorted triangles tend to produce elastic instability due to inaccurate evaluation of the local membrane curvature. Thus, we decided to adopt the simpler and more robust bending model of Wada *et al.*,^{34,35} with a bending coefficient k_b and bending energy

$$E_b = \sum_{i,j} 2k_b \tan^2 \left(\frac{\theta_{ij}}{2} \right), \quad (2)$$

where the summation is over all pairs of neighboring triangles i and j , and θ_{ij} is the angle between their normals. Note that this bending energy assumes zero spontaneous curvature for the membrane.

In addition, the red cells are known to conserve their surface area; and in our particle model, this is implemented through an energy penalty against local area dilatation

$$E_A = \frac{k_d}{2} \sum_j^N \left(\frac{A_0^j - A^j}{A_0^j} \right)^2 A_0^j, \quad (3)$$

where k_d is a constant, A_0^j is the undeformed area of the j th triangle, and the summation is over all N triangles of the RBC membrane. Finally, we include an energy penalty against the change of the total cell volume

$$E_V = \frac{k_v}{2} V_0 \left(\frac{V_0 - V}{V_0} \right)^2, \quad (4)$$

where k_v is a constant coefficient, and V_0 is the initial volume of the cell. Under large forcing and severe cell deformation, this volume constraint helps to prevent fluid particles from penetrating the membrane. The two constraints in Eqs. (3) and (4) are similar to those used by Discher *et al.*³⁶ and Fedosov *et al.*,⁸ but we have excluded their constraint on the total surface area. In all simulations, the cell surface area and volume are conserved to within 2%. Using Eqs. (1)–(4), we write the total elastic energy of the cell membrane as $E_m = E_s + E_b + E_A + E_V$ and calculate the elastic force acting on the membrane particles as

$$\mathbf{f}_m = -\partial E_m / \partial \mathbf{r}. \quad (5)$$

The elasticity of our discrete network of particles and springs can be related to continuum models for an elastic membrane by considering the limit of small strain. For a regular and isotropic triangular mesh, the network has an effective shear modulus $G_s = \frac{\sqrt{3}}{4} k_s$, Young's modulus $E = \frac{2}{\sqrt{3}} k_s$, Poisson ratio $\nu = \frac{1}{3}$, and area dilation modulus $K = \frac{\sqrt{3}}{2} k_s$.³⁷ The bending constant k_b can be related to the Helfrich coefficients as:³⁸ $k_b = 2\sqrt{3}(\kappa_c + \kappa_g/2) = 2\sqrt{3}\kappa$, κ_c and κ_g being the coefficients for the mean curvature and the Gaussian curvature terms in the Helfrich bending energy, and κ the average bending modulus.^{8,36} There is a small amount of nonuniformity in our tessellation, necessitated by the requirement of covering the curved biconcave surface of the RBC. This may have introduced small deviations from the above relationships. For nonlinear elasticity under large strain, Omori *et al.*³⁷ have compared the strain-hardening of spring networks with that of the continuum Skalak and Mooney-Rivlin models. For most of the simulations reported here, we have used a fixed bending constant $k_b = 6.93 \times 10^{-19}$ J, chosen according to Hochmuth and Waugh.³⁹ To examine the role of in-plane elasticity, we will vary the stretching constant k_s in a range consistent with measured shear modulus in healthy RBC and iRBC in different stages of infection. Based on such parameters, the ratio between the bending forces and the in-plane stretching forces can be estimated as $\xi = k_b / (a^2 k_s) = O(10^{-3})$, where a is the effective cell radius. Thus, bending contributes little to the membrane dynamics and RBC deformation.⁹

Finally, as is commonly done in the literature,^{28,40} we have also employed a repulsive potential to avoid solid-solid contact. Under large deformation, the cell membrane particles tend to penetrate into the wall or the parasite, e.g., when the cell squeezes through narrow channels. We adopt the cut-off spring model^{28,40} that uses a repulsive potential with a finite range and a linear elastic constant k_r . In our case, numerical experiments show that setting the range to the initial nearest-neighbor separation is a good choice. We have also tested different

k_r values and found that the results are insensitive to k_r within the range of 2×10^{-4} to 10^{-2} N/m. We have used $k_r = 2 \times 10^{-3}$ N/m for all the results reported.

B. Governing equations and numerical algorithm

As a tool for computing fluid flow, the SPH method has been used widely, and several comprehensive reviews have appeared in recent years.^{29,41} For our current purpose, we will only list the governing equations and outline the solution algorithm. In the SPH formalism, continuum governing equations are discretized onto particles more or less uniformly distributed in space. A kernel function is defined on each particle so that a continuous field for any physical quantity, including velocity, pressure, and density, can be constructed from the discrete particle values through spatial averaging. Although projection schemes are available for imposing incompressibility,^{42–44} we have adopted a weakly compressible scheme for simplicity. Thus, we have the following equations governing the motion of the particles:

$$\frac{D\rho}{Dt} = -\rho \nabla \cdot \mathbf{v}, \quad (6)$$

$$\frac{D\mathbf{v}}{Dt} = \frac{1}{\rho} \nabla \cdot \boldsymbol{\tau} - \frac{1}{\rho} \nabla p + \mathbf{f}_m, \quad (7)$$

$$\frac{p}{p_0} = \left(\frac{\rho}{\rho_0}\right)^7 - 1, \quad (8)$$

where D/Dt is the material derivative taken on each moving particle, $\boldsymbol{\tau}$ is the viscous stress tensor, and \mathbf{f}_m is the membrane force per unit mass from Eq. (5), and is zero for fluid and parasites particles. The particles that constitute the solid parasite move as a rigid body according to the total force and torque exerted by the surrounding cytosol. The reference density ρ_0 and reference pressure p_0 are chosen to ensure a high “speed of sound” and approximate incompressibility. These, together with adequate spatial resolution, maintain the density fluctuation to within 1% in all simulations. We advanced all particles explicitly by a two-step prediction-correction algorithm.³¹ The particle shifting strategy⁴⁵ is adopted to prevent tensile instability.

C. Cell geometries

For the healthy RBC, we adopt the biconcave shape specified by the formula of Evans and Fung,¹

$$T(r) = \sqrt{1 - (r/R_0)^2} [C_0 + C_1(r/R_0)^2 + C_2(r/R_0)^4], \quad (9)$$

where $T(r)$ is the thickness of the RBC as a function of distance r from the center axis, and R_0 is the radius of the RBC, measured from the center to the outer edge (Fig. 2). We have taken the following values: $R_0 = 3.9 \mu\text{m}$, $C_0 = 0.81 \mu\text{m}$, $C_1 = 7.83 \mu\text{m}$, and $C_2 = -4.39 \mu\text{m}$; the center has a thickness of $T_1 = 0.81 \mu\text{m}$ and the largest thickness at the rim is $T_2 = 2.4 \mu\text{m}$.

Through the various stages of infection, the iRBC changes its volume, shape, and surface area while the parasite grows in size. A survey of experimental measurements of iRBC and parasite dimensions reveals considerable variations not only among different studies but also among cells of the same cohort.^{6,14,15,46} We have strived to capture the overall trend of these data and adopted the dimensions in Table I. In the ring-stage, the shape and size of the iRBC do not differ appreciably from their healthy counterparts,¹⁵ and we have adopted the shape in Fig. 2 for the ring-stage iRBC as well. The merozoite is a disc of radius $R = 1 \mu\text{m}$ and thickness $h = 0.5 \mu\text{m}$. Drastic morphological changes of the iRBC occur in the trophozoite and schizont stages. During the trophozoite stage, the merozoite continuously digests cytoplasmic hemoglobin and grows from $2.0 \mu\text{m}$ to $4.0 \mu\text{m}$ in diameter. Meanwhile, the cell surface area remains within a narrow margin of variation.^{6,14,15,46} Thus, the growing parasite progressively

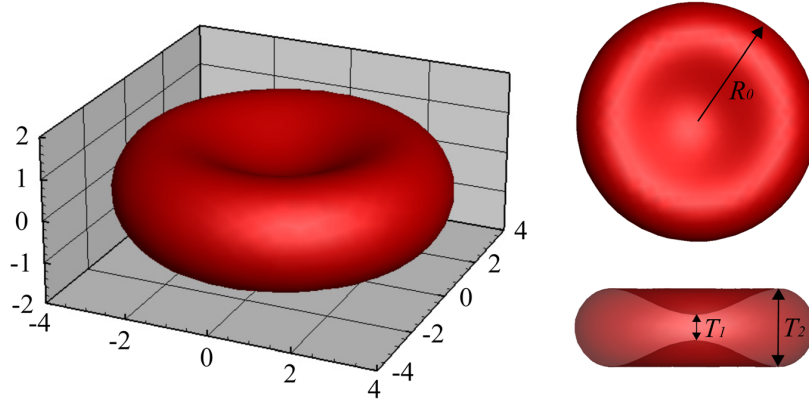


FIG. 2. The healthy RBC and the ring-stage iRBC have the same biconcave shape described by Eq. (9), with the smallest and largest thickness being $T_1 = 0.81 \mu\text{m}$ and $T_2 = 2.4 \mu\text{m}$. The spatial coordinates are marked in microns.

swells the cell and gives it an asymmetric biconcave shape. Here, we represent the iRBCs at the early and late trophozoite stages by the shapes of Fig. 3, with the merozoite being a sphere of increasing radius R . In the schizont stage, the iRBC undergoes a marked reduction in volume and surface area and assumes a more or less spherical shape.^{14,15,47,48} The merozoites multiply and form a tightly packed cluster that may occupy as much as 80% of the iRBC's volume.^{4,15} We represent the schizont-stage iRBC as a spheroid with radius of $3.2 \mu\text{m}$ and thickness of $4 \mu\text{m}$ (Fig. 4). The cluster of merozoites is modeled as a single spheroidal particle of the same aspect ratio as the iRBC, with radius $R = 2.4 \mu\text{m}$ and thickness $h = 3 \mu\text{m}$.

The bending energy introduces a subtlety in realizing the prescribed cell shapes in our particle-spring model. At the start of a simulation, we initialize the resting length of all springs to that corresponding to the tessellation of the underformed cell surface. This relieves all in-plane stretching. For the healthy and ring-stage cells, the shape of Eq. (9) is very close to a minimizer of the bending energy.^{33,49} Therefore, turning on the bending energy induces less than 2% of adjustment in the cell dimensions. For the trophozoite and schizont stages, on the other hand, the chosen iRBC geometries differ considerably from the bending-energy minimizer. This does not constitute a complication in practice because, as explained in Sec. II A, cell deformation will be dominated by hydrodynamic forces and in-plane elasticity in our simulations, and bending has negligible effects.

III. VALIDATION: SIMULATION OF TANK-TREADING

Hosseini and Feng^{9,50} have previously tested several aspects of particle-based RBC models. In this section, we simulate the tank-treading motion of the red cell in a simple shear flow as a validation of our cell model, numerical algorithm, and resolution. This is one of several modes of motion for a red cell in shear flow, and occurs at high shear rates.⁵¹ The cell is elongated to

TABLE I. Dimensions of the healthy and infected red cell in different stages. $s_e = S/(4\pi a^2)$ denotes the *excess surface area ratio* of the cell, where a is the effective cell radius defined as the radius of a sphere having the volume V of the cell. The last column indicates the dimensions of the parasite.

Case	$S (\mu\text{m}^2)$	$V (\mu\text{m}^3)$	s_e	$a (\mu\text{m})$	Parasite (μm)
Healthy	132	92	1.34	2.80	(none)
Ring	132	92	1.34	2.80	$R = 1, h = 0.5$
Early trophozoite	132	105	1.23	2.92	$R = 1.4$
Late trophozoite	132	116	1.15	3.02	$R = 1.7$
Schizonte	97	85	1.04	2.72	$R = 2.4, h = 3$

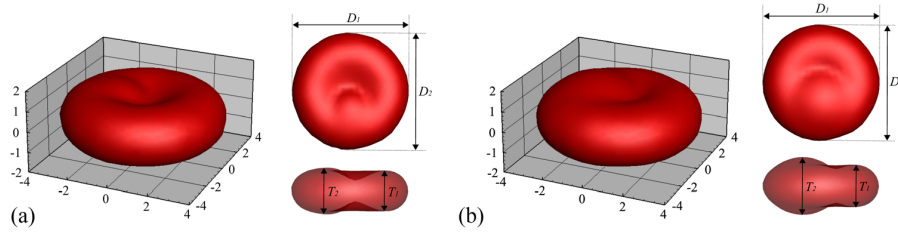


FIG. 3. The cell geometries at (a) the early trophozoite stage, with $(D_1, D_2, T_1, T_2) = (7.77, 7.76, 2.7, 3.0) \mu\text{m}$, and (b) the late trophozoite stage, with $(D_1, D_2, T_1, T_2) = (7.80, 7.72, 2.8, 4.0) \mu\text{m}$.

a cigar-like shape and its membrane rotates around the cytoplasm at a frequency that is linearly proportional to the shear rate of the flow.⁵²

Our numerical results will be compared with those of Sui *et al.*,⁵³ a careful computational study using the immersed boundary method in a lattice Boltzmann framework. The geometric setup and key physical parameters are matched between the two studies. The computational domain has dimensions $L_x \times L_y \times L_z = 6.4a \times 5a \times 5a$. The flow is in the x direction, driven by the motion of the top and bottom walls ($z = \pm 2.5a$) at a constant velocity in opposite directions. On the boundaries in the flow direction ($x = \pm 3.2a$) and the neutral direction ($y = \pm 2.5a$), we impose periodic boundary conditions. A healthy red blood cell is placed at the center of the computational domain with an initial tilt angle of $\pi/4$. The cell shape is given by Eq. (9) and its effective radius is $a = 2.8 \mu\text{m}$.

We match the following dimensionless groups with Sui *et al.*:⁵³ the cytosol-to-surrounding-fluid viscosity ratio $\lambda = \mu_c/\mu = 1$, density ratio $\rho_c/\rho = 1$, and the capillary number $Ca = \mu a K/G_s$, where G_s and K are the shear modulus of the membrane and the shear rate, respectively. Inertia is negligible in both studies; the Reynolds number $Re = \rho K a^2/\mu$ is fixed at 0.1 in Sui *et al.*,⁵³ and varies between 0.014 and 0.072 in our simulations. For membrane elasticity, Sui *et al.*⁵³ employed the continuum model of Skalak *et al.*⁵⁴ for in-plane deformation, and neglected bending altogether. For a meaningful comparison, we have matched the in-plane shear modulus G_s of our elastic network to that of the Skalak model at the limit of small strain and carried out simulations with and without bending. In the former case, we have used a physiologically appropriate bending constant $k_b = 6.93 \times 10^{-19} \text{ J}$,³⁹ which gives a ratio between the bending and shear moduli $\xi = k_b/(a^2 k_s) = 7.4 \times 10^{-3}$, indicating a negligible role of bending relative to in-plane elasticity. Finally, to test convergence with spatial resolution, we have used a coarse resolution (with $N_p = 440$ membrane particles and a nominal particle spacing of $l_0 = 0.6 \mu\text{m}$) and a fine resolution ($N_p = 1058$, $l_0 = 0.4 \mu\text{m}$). The total number of particles are 21698 and 63287, respectively.

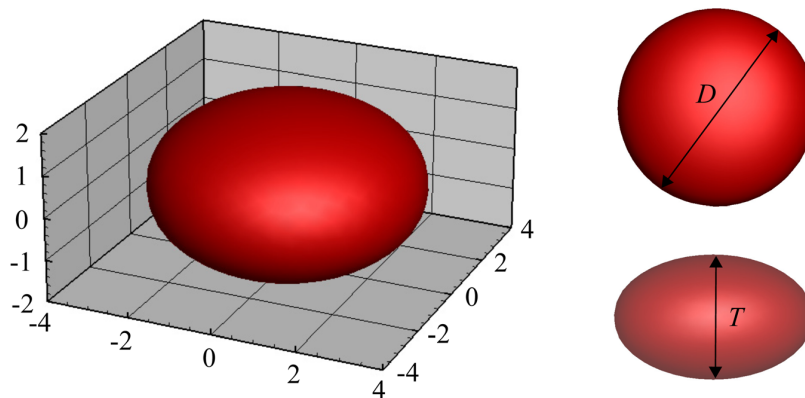


FIG. 4. The iRBC has a spheroidal shape at the schizont stage, with diameter $D = 6.4 \mu\text{m}$ and thickness $T = 4 \mu\text{m}$.

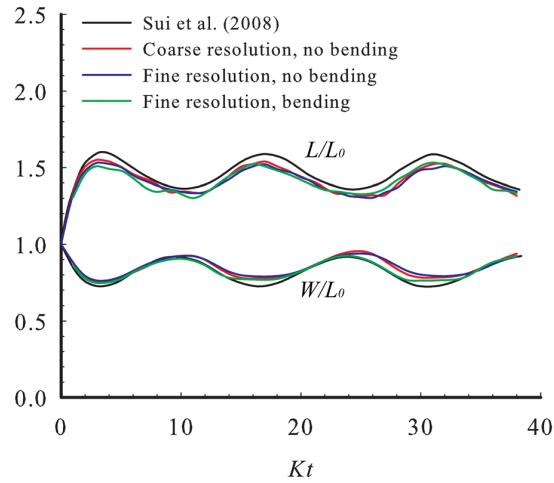


FIG. 5. Tank-treading: temporal evolution of the cell length L and width W for $Ca = 0.93$. Three of our simulations, at coarse and fine spatial resolutions with and without bending, are compared with the result of Sui *et al.*,⁵³ which does not include bending elasticity.

Following Sui *et al.*,⁵³ we have tested four Ca values from 0.57 to 2.8. In this range, the RBC executes a tank-treading motion of increasing frequency, with the cell being more elongated at higher Ca . Figure 5 depicts the temporal evolution of the cell's length L and width W for $Ca = 0.93$. First, the bending elasticity affects the cell shape and motion only slightly; it changes the cell length by less than 1% and increases the frequency of tank-treading by approximate 3%. Second, the numerical results obtained at the coarse and fine resolutions differ by less than 1%. This confirms convergence of the simulation with respect to the number of particles. Finally, our numerical results are in close agreement with that of Sui *et al.*⁵³ We have accurately captured the oscillation of the cell's length and width during tank-treading. But quantitative discrepancies can be discerned; our model slightly underestimates the deformation of the cell both in L and W .

To compare the simulations at different Ca values, we plot in Fig. 6 the time-averaged values of L and W as well as the period of tank-treading as functions of Ca . For \bar{L} and \bar{W} , the agreement is excellent throughout the Ca range. On the other hand, our frequency f is mostly lower than that predicted by Sui *et al.*,⁵³ and the discrepancy increases with Ca . For example, our f at fine resolution without bending falls below that of Sui *et al.*⁵³ by 1.4% to 12.8% as Ca increases from 0.57 to 2.8. Bending elevates the frequency slightly by 3.9% at $Ca = 0.57$ and 1.8% at $Ca = 2.8$. A possible cause of this discrepancy is the different constitutive models used in the two simulations. With larger deformation at higher Ca , the strain-hardening in the Skalak

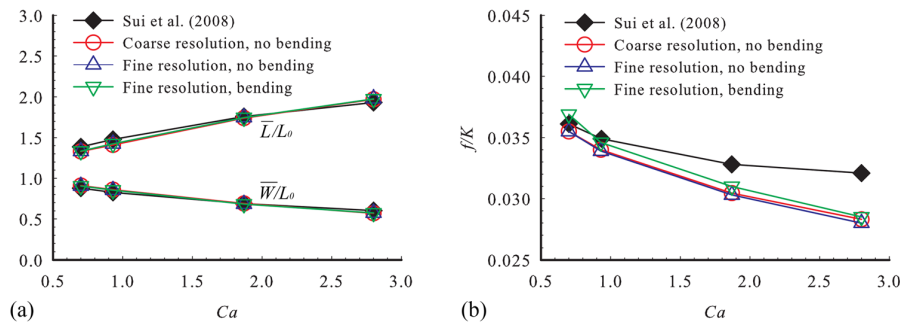


FIG. 6. (a) The average RBC length \bar{L} and width \bar{W} as functions of the capillary number Ca . (b) The dimensionless frequency f of tank-treading, scaled by the shear rate K , as a function of the capillary number Ca .

model becomes more pronounced than in our spring network model. However, it is unclear why this difference does not manifest itself as strongly in the dimensions of the cell.

IV. RESULTS

The computational domain is schematically depicted in Fig. 7. The geometry and dimensions of the microfluidic channel are inspired by recent experimental setups.^{10,12,22,23} The total length of the domain is $L = 24 \mu\text{m}$. The entrance has a rectangular cross section of width $W = 12 \mu\text{m}$ and height $H = 4.8 \mu\text{m}$. The same height is maintained throughout the entire conduit, but the width contracts through a 45° shoulder to a narrower width w . The length of the narrow segment is fixed at $l = 8 \mu\text{m}$, but its width takes on one of three values, $w = 3.2, 4$ and $4.8 \mu\text{m}$, which will be called the narrow, medium, and wide channels, respectively. Further downstream is a sudden expansion to a cross-section that is identical to the one at the entrance. The red cell always enters “edgewise,” that is, with its circular mid-plane horizontal and midway between the top and the bottom of the microchannel in the schematic.

Based on physiological values,^{55,56} we have set the density and viscosity of the blood plasma (or surrounding fluid in the microfluidic channel) to be $\mu = 10^{-3} \text{ Pa} \cdot \text{s}$ and $\rho = 10^3 \text{ kg/m}^{-3}$. In healthy red cells, the cytosol viscosity is typically 3–6 folds higher than the plasma viscosity because of the hemoglobin and other proteins in the cytosol.⁵⁷ This viscosity ratio can affect the cellular dynamics.⁵⁸ Moreover, during malaria development, the parasite continually digests the hemoglobin. Thus, the cytosol viscosity may evolve in time, although no quantitative results have been found in the literature. For simplicity, we have assigned equal viscosity to the cytosol and the plasma ($\lambda = 1$) as did many previous simulations.^{25,53,59} Besides, the density of all fluid and solid components is set to $\rho = 10^3 \text{ kg/m}^{-3}$.

To simulate a pressure-driven flow through the microchannel, we impose periodic boundary conditions between the entrance and the exit of the channel, and apply a constant body force on all the particles to drive the flow. The body force per unit mass F_x can be related to the effective pressure drop across the length of the channel as such: $\Delta P = \rho F_x L$. This setup is preferable to imposing a pressure gradient directly because the SPH methodology handles the periodic boundary conditions more easily.⁴³ From this pressure drop, we can define a characteristic velocity $U = \Delta P w^2 / (8 \mu L)$ and a characteristic time $T = L/U$. Now a capillary number can be defined as

$$Ca = \frac{\mu U}{G_s}. \quad (10)$$

In the results to be presented below, we fix ΔP to be 12 Pa, on the same order of magnitude as in recent microfluidic experiments on iRBC deformability.^{11,12} Under these conditions, Ca lies

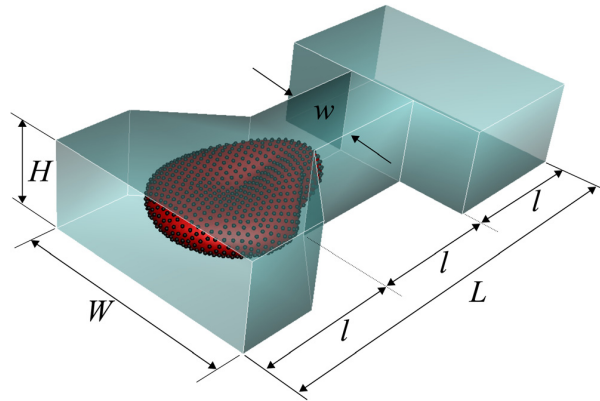


FIG. 7. Schematic of the computational domain. The overall dimensions of the channel are $L = 24 \mu\text{m}$, $W = 12 \mu\text{m}$, and $H = 4.8 \mu\text{m}$, with three segments of equal length $l = 8 \mu\text{m}$. The narrow section in the middle has a width $w = 3.2, 4$, and $4.8 \mu\text{m}$ for the narrow, medium, and wide channels.

between 2.56×10^{-3} and 2.88×10^{-2} for the range of w and G_s values to be examined. The Reynolds number, defined using the characteristic velocity U and the effective cell radius a , is on the order of 10^{-3} .

To establish numerical convergence of the results with respect to spatial resolution, we have simulated passage of the healthy RBC through the wide channel ($w = 4.8 \mu\text{m}$) using two resolutions. The coarse resolution has a nominal particle separation $l_0 = 0.6 \mu\text{m}$, with 440 particles on the RBC membrane and 10 977 particles overall. For the fine resolution, $l_0 = 0.4 \mu\text{m}$ and we deploy 1058 particles on the membrane and 29 648 particles overall. The cell trajectories for these two cases agree within 3% throughout the passage, and the overall transit time differs by less than 5%. We have further checked the cell shape and the membrane strain contours, and the differences between the two cases are very small. All subsequent results are presented using the fine resolution.

As explained in the Introduction, the rigidification of iRBCs has three potential causes, the stiffness of the membrane, the cell geometry, and the internal components, including the shape and size of the merozoite. In the following, we will first investigate each element separately while fixing the other parameters at baseline values. Then, we will combine all three changes together as occurs during a real infection, and examine how the overall rigidity of the iRBC evolves through the ring, trophozoite, and schizont stages.

A. Effect of the membrane stiffness

According to prior measurements using micropipette aspiration, the healthy RBC has a membrane shear modulus around $5 \mu\text{N/m}$.^{6,60} After infection by malaria, the merozoites export parasitogenic proteins onto the membrane that remodel the spectrin network.^{61,62} A direct consequence of this modification is an increase in the membrane rigidity. Experimental evidence^{6,13} shows that the shear modulus of the membrane remains largely constant through the ring, trophozoite, and schizont stages between 15 and $25 \mu\text{N/m}$. In this subsection, we fix the resting shape of the cell to that of the healthy RBC, and systematically examine the effect of increasing the shear modulus G_s , from $5 \mu\text{N/m}$ to $35 \mu\text{N/m}$. No merozoite will be included inside the cell. Specifically, we will study the passage or arrest of the cells in the wide, medium, and narrow microchannels. The change in G_s is effected by varying the stretch constant k_s of the springs in our particle-spring network. The Young's modulus and area dilation modulus will change simultaneously as well.

Figure 8 depicts the transit of the RBC through the narrow channel at three values of the shear modulus. Similar trends are seen in the medium and wide channels. The instantaneous position of the RBC is indicated by x_c , the longitudinal coordinate of the centroid of all

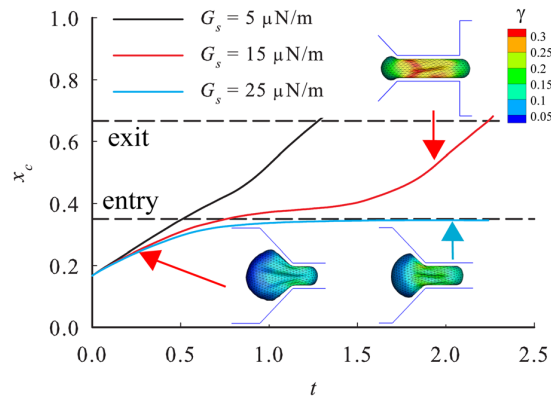


FIG. 8. The trajectories of RBCs through the narrow channel ($w = 3.2 \mu\text{m}$) for three values of the shear modulus G_s . The insets show top-view snapshots of the cell during the transit with color contours of the local stretching γ of Eq. (11), at $t = 0.27$ and $t = 1.9$ for $G_s = 15 \mu\text{N/m}$ (red arrows) and at $t = 2.1$ for $G_s = 25 \mu\text{N/m}$ (blue arrow).

membrane particles, scaled by the channel length L . Time is scaled by the characteristic time T . The horizontal dashed lines indicate the entry and exit to the narrow middle segment. Since the undeformed RBC has a diameter of $7.8 \mu\text{m}$, more than twice the width of the narrow passage, the cell undergoes large deformations. The cell with the softest membrane ($G_s = 5 \mu\text{N/m}$) passes through the contraction readily, while the one with the intermediate G_s takes longer time. The cell with the highest membrane modulus ($G_s = 25 \mu\text{N/m}$) fails to traverse the channel; it blocks the entry to the narrow segment. The insets show snapshots for the latter two runs. On the surface of the cell, we have superimposed contour plots of the local deformation γ . For the i th membrane particle, γ_i is defined by averaging the deformation of all the N_i springs connected to it,

$$\gamma_i = \sqrt{\frac{\sum_{j=1}^{N_i} \left(\frac{L_{ij}}{L_{ij,0}} - 1 \right)^2}{N_i}}, \quad (11)$$

where L_{ij} and $L_{ij,0}$ are the current and resting lengths of the springs. Generally, the membrane suffers large shear deformation in the dimple region, i.e., the thin central area of the undeformed RBC, and relatively small strains at the rim. The stretching γ can reach 30% for $G_s = 15 \mu\text{N/m}$ after the cell enters the narrow channel completely. Also, we notice that the squeezing has produced one or more longitudinal wrinkles on the membrane, typically at the central dimple. Because of the slight asymmetry in the initial tessellation of the surface, the wrinkle and the stretching contour appear slightly asymmetric.

The most obvious effect of G_s is in slowing down the transit. This is evident from comparing the trajectories for $G_s = 5 \mu\text{N/m}$ and $15 \mu\text{N/m}$ in Fig. 8. To be more quantitatively, we define a transit time t_t as the interval that starts with the cell's forefront reaching the entry and ends with its centroid leaving the exit. Figure 9 plots the transit time as a function of the membrane shear modulus for the three channels. Membrane rigidity is seen to lengthen the transit time in all channels. Moreover, this effect becomes more pronounced for narrower channels. For the wide and medium channels ($w = 4.8$ and $4 \mu\text{m}$), increasing G_s from 5 to $35 \mu\text{N/m}$ increases t_t by about 20% and 30%, respectively. For the narrow channel ($w = 3.2 \mu\text{m}$), on the other hand, t_t diverges at $G_s = 25 \mu\text{N/m}$; the cell blocks the channel and fails to pass.

Cell blockage at $G_s = 25 \mu\text{N/m}$ indicates that the supplied ΔP , corresponding to $Ca = 4 \times 10^{-3}$ in this case, is insufficient to deform the cell to the extent required for passage. Numerical experiments show that doubling ΔP will lead to passage of this cell. Thus, there exists a *critical pressure* for passage between these two situations, and such a pressure is expected to correlate directly with the membrane modulus. Previously, Ma and coworkers^{12,22,23}

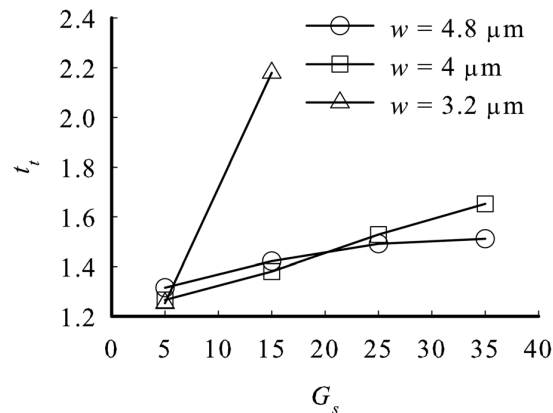


FIG. 9. The transit time t_t , made dimensionless by T , as a function of the membrane shear modulus G_s for the three channels.

have used such a critical pressure to probe the *cortical tension* of red blood cells. This tension is assumed to be constant in the membrane, regardless of the local deformation, and is extracted from the critical pressure drop via the Young-Laplace equation. With the help of simulations that properly account for the membrane elasticity, a similar procedure can be developed as a means of measuring the cell membrane modulus.

We end this subsection by pointing out a subtle feature of the blockage. In microfluidic experiments, blockage is often incomplete. Because of the bending elasticity of the membrane, the corners of the typically rectangular cross-section may not be blocked, and a fluid flow persists through these small openings.^{10,12,63} Our simulations appear also to show a thin gap between the wall and the cell membrane; see insets of Fig. 8. This clearance is due to the repulsive force between the cell membrane and the wall and is roughly equal to the nominal particle separation l_0 . Thus, it is too small for particles to slip through, even at the corners, and the blockage of the microchannel is complete. This subtle difference between experimental and computational blockage may lead to potential errors in predicting the cell stiffness.⁶⁴

B. Effect of the cell geometry

In the ring stage, the malaria-infected RBC retains the shape and size of the healthy RBC. Advancing into the trophozoite and the schizont stages, however, it undergoes dramatic morphological changes (cf. Table I). Overall, the transformation can be viewed as a steady loss of the excess surface area, as the cell becomes increasingly swollen.⁴⁸ In this subsection, we investigate the passage and blockage of iRBCs having the four shapes indicated in Table I for the ring, early trophozoite, late trophozoite and schizont stages. The shear modulus is fixed at $G_s = 15 \mu\text{N}/\text{m}$ according to prior measurements.^{6,13} Although we will refer to these cell morphologies by the stages of infection, the cells have no merozoite inside.

Consider the narrow channel first, with a width of $w = 3.2 \mu\text{m}$ in the mid-section. Our simulations show that only the ring-stage iRBC can pass, and all the other cell shapes block the channel. Figure 10 depicts the steady-state shape of the iRBC after blockage. Once the iRBC is arrested at the contraction, the negative pressure downstream draws out a tongue from the cell membrane, whose length l_t is plotted as a function of the excess surface area ratio s_e . With the loss of excess surface area, l_t decreases monotonically. Much as in micropipette aspiration, this indicates a gradual loss of the cell's deformability. Increasing the pressure drop ΔP will deform the cell more and produce a longer protrusion. However, within the range tested in our numerical experimentation, we were unable to deform any of the three shapes sufficiently, so that it passes the narrow channel.

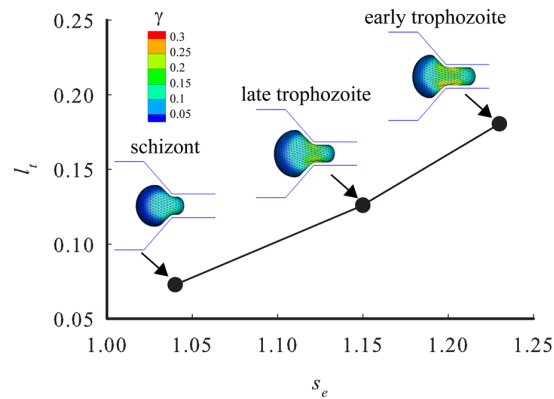


FIG. 10. Steady-state shape of the iRBC in the early trophozoite, late trophozoite, and schizont stages after it blocks the narrow channel ($w = 3.2 \mu\text{m}$). The length of the tongue l_t , defined as the distance between the cell front and the channel entry and scaled by the channel length L , is plotted as a function of the excess surface area ratio s_e . Color contours of the surface stretching γ are also shown in the insets.

In this connection, it is interesting to note the concept of minimum cylindrical diameter (MCD) that has been used to interpret recent experiments on cell entry into microfluidic channels.^{65–67} Because of its fixed surface area and volume, a red cell can at most be stretched into a cylinder of a certain length and diameter, and thus would fail to enter a thinner capillary regardless of the magnitude of forcing. In our view, the MCD thus defined is not an optimal indicator of cell blockage of capillaries. It is a purely geometric lower-bound that does not account for the dynamic aspects of the passage process. For instance, in microfluidic channels as well as *in vivo*, the pressure gradient available is of finite magnitude. Thus, blockage may appear in channels much wider than MCD, far before the cell is stretched into a cylindrical shape (cf. insets in Figs. 8 and 10). Numerical experiments show this to be the case, especially for relatively high values of the membrane modulus. Besides, MCD is defined for a cylindrical tube and does not apply to passage through the narrow slit in the spleen nor through microfluidic channels having rectangular cross-sections.

In the medium and wide channels, most of the four iRBC shapes pass without occlusion. The sole exception is the schizont-stage iRBC blocking the medium channel. Figure 11 plots the cell transit time t_t as a function of s_e . From the ring stage ($s_e = 1.34$) to the late trophozoite stage ($s_e = 1.15$), the cell surface area remains more or less constant while the cell volume increases (Table I). Consequently, t_t increases monotonously with decreasing s_e in both channels as the gradual swelling of the cell makes deformation more difficult. The schizont shape, more spherical with the lowest $s_e = 1.04$, corresponds to much reduced cell volume and surface area. This decreases deformability and causes blockage of the medium channel. Through the wide channel, on the other hand, not only does the schizont-iRBC manage to pass but it takes the least transit time among all cases. This anomaly is mainly due to the much smaller cell volume of the schizont shape; the iRBC barely needs to deform in order to enter the contraction. To sum up, the excess surface area ratio s_e is a key determinant of cell deformability, especially when large deformation is required for passing narrow pores. In relatively wide channels, the cell size also plays a role.

C. Effect of the parasites cluster

Through the three stages of malaria infection, the parasite changes shape and increases in size, eventually taking up more than half of the volume of the host red cell in the schizont stage.^{14,15} In this subsection, we focus on the effect of the parasite volume on transit of the iRBC through a microfluidic channel. In the ring stage, the merozoite develops into a disc $2\ \mu\text{m}$ in diameter and $0.5\ \mu\text{m}$ in thickness. Simulations show that the ring-stage iRBC can pass through all three channels. This agrees with the observations of Shelby *et al.*¹⁰ in microfluidic channels of similar size (Fig. 1) and is also consistent with the conclusion of Hosseini and Feng⁹ that the ring-stage merozoite is too small to hinder cell deformation in stretching simulations.

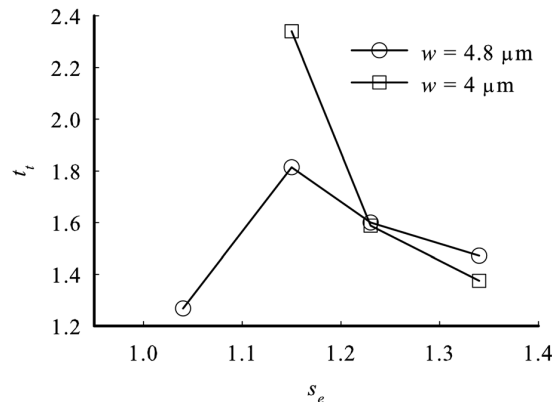


FIG. 11. The transit time t_t through the medium and wide channels as functions of the excess surface area ratio s_e . The transit time is scaled by T .

In trophozoite and schizont stages, we have systematically varied the parasite size for each of the iRBC shapes of Figs. 3 and 4 and Table I, with the membrane shear modulus fixed at $G_s = 15 \mu\text{N/m}$. A clear trend emerges for all three channels: increasing parasite size eventually causes blockage, and the minimum parasite size increases for blocking wider channels. In the following, we will only present results of the schizont iRBC in the wide channel ($w = 4.8 \mu\text{m}$), with the iRBC having a spheroidal shape and containing a rigid spheroidal parasite of the same aspect ratio 1.6 (Fig. 4). In reality, the parasite multiplies into dozens of merozoites closely packed inside a digestive vacuole at the center of the iRBC.^{4,68} Our spheroidal parasite represents the entire vacuole. The iRBC radius is fixed at $3.2 \mu\text{m}$, and we vary the radius of the parasite from 1.6 to $2 \mu\text{m}$.

Figure 12 shows the trajectories of the iRBC for two sizes of the parasite. A baseline case with no parasite is also shown for comparison. Not surprisingly, having the parasite slows down the passage. With the large parasite, the iRBC blocks the constriction. Note that in this case, the parasite is still considerably smaller than the channel size. The occlusion is not due directly to the solid parasite blocking the channel, but indirectly to the parasite constraining the deformation of the cell. The membrane presses against the solid parasite and deforms less as a result, a scenario previously analyzed in stretching of iRBC by optical tweezers.⁹ Recall that membrane-parasite overlap is prohibited in our model by a repulsive potential. As one may expect, the critical parasite size for occlusion decreases for narrower channels and higher membrane stiffness.

It is interesting to point out that a smaller parasite tends to move forward inside the cell during the transit and ends up in the front part of the cell (see top inset in Fig. 12). A larger parasite, on the other hand, feels the resistance from the constricting channel walls. It tends to move more slowly and shift toward the rear portion of the cell. In particular, when blockage happens, the parasite is pushed against the rear end of the membrane (see bottom inset in Fig. 12). Conceivably, this is a precursor to “pitting,” when the parasite is expelled from the cell through a temporary opening in the membrane. Such a process has been observed *in vivo*⁶⁹ and in microfluidic channels.¹⁰

D. Combinations

In this subsection, we integrate all three factors examined above, stiffening of the cell membrane, changes in cell morphology and parasite growth, into a series of simulations that mimic the evolution of iRBC through the various stages of infection. Following microfluidic experiments,^{10,12,65,67} we correlate the appearance of blockage in channels of different width with the overall loss of deformability. For the healthy red cell, we take $G_s = 5 \mu\text{N/m}$; while for all stages of infection, we use a constant $G_s = 15 \mu\text{N/m}$ in accordance to prior measurements

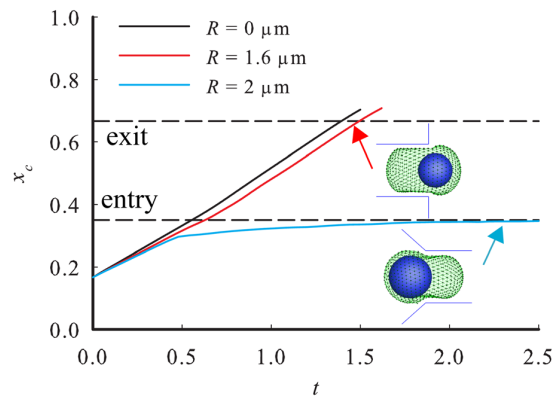


FIG. 12. Trajectories of the schizont-stage iRBC in the wide channel ($w = 4.8 \mu\text{m}$) with a parasite of different sizes. $R = 0$ indicates a baseline case without parasite, and the insets are snapshots of the parasite configuration for the other two trajectories.

TABLE II. The passage and blockage of healthy and infected red blood cells through microfluidic channels of different size.

	$w = 3.2 \mu\text{m}$	$4 \mu\text{m}$	$4.8 \mu\text{m}$
Healthy	passage	passage	passage
Ring	passage	passage	passage
Early trophozoite	blockage	blockage	passage
Late trophozoite	blockage	blockage	passage
Schizont	blockage	blockage	blockage

and computations.^{6,9,13} The shape and size of the iRBC and the parasite are those of Table I and Figs. 2–4. Note that we differentiate between the early and late trophozoite stages.

Inspired by images from the microfluidic experiments of Shelby *et al.*¹⁰ (Fig. 1), we summarize our results in a tabular form (Table II). Evidently, with the progression of malaria infection, the iRBC gradually loses its deformability and causes blockage of larger and larger channels. The healthy RBC is able to pass through all three channels used in the current study. So is the iRBC in the ring stage. Infected red cells in the early and late trophozoite stages pass through the wide channel but block the medium and narrow ones. In the schizont stage, the iRBC blocks even the wide channel. These results are in qualitative agreement with the experiment of Shelby *et al.*¹⁰ In fact, one may even claim a degree of quantitative agreement. For example, they reported that trophozoite-stage iRBCs block a channel $4 \mu\text{m}$ in width but pass freely through a $6 \mu\text{m}$ channel, and schizont-stage iRBCs block a $6 \mu\text{m}$ channel but traverse a $8 \mu\text{m}$ channel. However, we should note that our channel geometry and pressure drop have not been precisely matched with those in the experiment. Incidentally, Shelby *et al.*¹⁰ also observed an interesting phenomenon of “jamming,” with two or more cells clogging the contraction leading to the narrow part of the flow conduit (Fig. 1). In this case, the adhesion among iRBCs plays an important role in causing the blockage. Since our simulation deals only with single red cells, we cannot capture the jamming phenomenon.

V. CONCLUSION

In this article, we report a smoothed-particle-hydrodynamics simulation of the transit of healthy and malaria-infected red blood cells through microfluidic channels. The main conclusion is that with progression of the malaria infection, the red cell gradually loses its deformability, measured by its ability to pass through a microchannel of a certain dimension. In our discrete model, the cell membrane is represented by a particle-spring network that possesses in-plane elasticity as well as bending elasticity. The parasite is modeled by a group of particles constrained to move as a rigid body. The cytosol and surrounding liquid are discretized into standard SPH particles, and the entire fluid-solid system is simulated by an explicit SPH algorithm. The main objective of the work is to probe how changes in the cell membrane rigidity, the excess surface area of the cell and the size of the parasite, individually and taken together, affect the transit of the infected red cell through a microfluidic channel. Within the parameter ranges explored, the results can be summarized as follows:

- (a) The rigidity of the cell membrane hinders passage of the cell through microfluidic channels. The transit time increases with increasing membrane modulus, especially for the narrower channels. Blockage occurs for sufficiently stiff membranes. These results agree qualitatively with experimental observations.¹²
- (b) The progressive loss of excess surface area impairs the capability of the infected red cell in traversing narrow channels, and blockage occurs for sufficiently low excess surface area ratio. This agrees qualitatively with previous microfluidic experiments.^{6,7}
- (c) The presence of the parasite reduces the deformability of infected red cells, and the effect increases as the parasite grows. The parasite may cause occlusion of microfluidic channels

considerably larger than the parasite size. This result confirms previous speculations⁶ and is consistent with prior computational studies of cell stretching.⁹

- (d) In reality, all three factors are at play, and the numerical simulations successfully reproduce the experimental picture of infected red cells occluding larger and larger channels with the progression of infection. However, it is not straightforward to quantify the separate contribution of each factor and make a meaningful comparison among them.
- (e) The numerical simulations suggest that red cell rigidification at different stages of infection can be quantified by measuring the critical pressure drop required for passage through a constricting channel of a certain geometry. This provides a basis for developing microfluidic cell assays.

We should point out the assumptions and simplifications in our model that may have limited the fidelity and accuracy of the numerical results. The actual RBC membrane has a complex structure, and only the grossest features are retained in our particle-spring network. For one, infected red cells often present an irregular surface morphology, with spikes and knobs (cf. Fig. 1). The structural changes underlying such shapes are not accounted for in our model. We enforce areal conservation via an *ad hoc* energy penalty, not from the intrinsic constitutive behavior of the membrane. A potential remedy to this is to employ nonlinear springs that generate stronger strain-hardening for the membrane as a whole.³⁷ In addition, we have omitted membrane viscosity altogether. Prior work has indicated an essential role for this viscosity in determining the timescale of the membrane relaxation.⁵⁹ Moreover, we have assumed equal viscosity for the cytosol and suspending fluid for simplicity. In reality, the cytosol viscosity is considerably higher than that of the plasma⁵⁷ and may evolve dynamically as the parasite modifies the chemical composition of the cytosol. Finally, this study has focused on the deformability of infected red cells and disregarded cytoadherence, another important factor in the pathogenesis of malaria.⁸ Pathologically enhanced adherence among infected red cells and with the vascular endothelium plays a definite role in obstruction of microcapillaries, as experiments in microfluidic channels have already suggested.¹⁰ In future work, these simplifications should be examined and possibly removed in more sophisticated and faithful simulations.

Toward the goal of quantifying the deformation of healthy and infected red cells in microfluidic channels, this paper represents an initial step: we have proposed and investigated a computational model that is numerically reliable but drastically idealized in its physical elements. The logical next step is to compare its predictions with *in vitro* experiments. This will allow one to assess the validity of the physical assumptions in the model. We have barely addressed this issue in the current study and will devote a separate effort to it. Only after establishing a realistic and accurate computational model, we can hope to turn the microfluidic channel into a quantitative tool for analyzing cell properties.

ACKNOWLEDGMENTS

We thank Quan Guo, Thurston Herricks, and Hong Ma for helpful discussions. T.W. also thanks Giovanni Ghigliotti for suggestions on membrane models, Majid Hosseini for advice on the SPH code, and Dingyi Pan for sharing his knowledge on parallel computing. The study was supported by NSERC, the Canada Research Chair program, and the Canada Foundation for Innovation, and the computation was carried out at WestGrid.

¹E. Evans and Y. Fung, "Improved measurements of the erythrocyte geometry," *Microvasc. Res.* **4**, 335–347 (1972).

²H. Cranston, C. Boylan, G. Carroll, S. Suter, J. Williamson, I. Gluzman, and D. Krogstad, "Plasmodium falciparum maturation abolishes physiologic red cell deformability," *Science* **223**, 400–403 (1984).

³N. Mohandas and E. Evans, "Mechanical properties of the red cell membrane in relation to molecular structure and genetic defects," *Annu. Rev. Biophys. Biomol. Struct.* **23**, 787–818 (1994).

⁴E. Hanssen, P. J. McMillan, and L. Tilley, "Cellular architecture of Plasmodium falciparum-infected erythrocytes," *Int. J. Parasitol.* **40**, 1127–1135 (2010).

⁵L. H. Miller, D. I. Baruch, K. Marsh, and O. K. Doumbo, "The pathogenic basis of malaria," *Nature* **415**, 673–679 (2002).

⁶G. B. Nash, E. O'Brien, E. C. Gordon-Smith, and J. A. Dormandy, "Abnormalities in the mechanical properties of red blood cells caused by Plasmodium falciparum," *Blood* **74**, 855–861 (1989).

- ⁷M. Dao, C. T. Lim, and S. Suresh, "Mechanics of the human red blood cell deformed by optical tweezers," *J. Mech. Phys. Solids* **51**, 2259–2280 (2003).
- ⁸D. A. Fedosov, B. Caswell, S. Suresh, and G. E. Karniadakis, "Quantifying the biophysical characteristics of *Plasmodium-falciparum*-parasitized red blood cells in microcirculation," *Proc. Natl. Acad. Sci. U.S.A.* **108**, 35–39 (2011).
- ⁹S. M. Hosseini and J. J. Feng, "How malaria parasites reduce the deformability of infected red blood cells," *Biophys. J.* **103**, 1–10 (2012).
- ¹⁰J. P. Shelby, J. White, K. Ganesan, P. K. Rathod, and D. T. Chiu, "A microfluidic model for single-cell capillary obstruction by *Plasmodium falciparum*-infected erythrocytes," *Proc. Natl. Acad. Sci. U.S.A.* **100**, 14618–14622 (2003).
- ¹¹H. Bow, I. V. Pivkin, M. D. Silva, S. J. Goldfless, M. Dao, J. C. Niles, S. Suresh, and J. Han, "A microfabricated deformability-based flow cytometer with application to malaria," *Lab Chip* **11**, 1065–1073 (2011).
- ¹²Q. Guo, S. J. Reiling, P. Rohrbach, and H. Ma, "Microfluidic biomechanical assay for red blood cells parasitized by *Plasmodium falciparum*," *Lab Chip* **12**, 1143–1150 (2012).
- ¹³F. K. Glenister, K. M. Fernandez, L. M. Kats, E. Hanssen, N. Mohandas, R. L. Coppel, and B. M. Cooke, "Functional alteration of red blood cells by a megadalton protein of *Plasmodium falciparum*," *Blood* **113**, 919–928 (2009).
- ¹⁴A. Esposito, J. Choimet, J. Skepper, J. Mauritz, V. Lew, C. Kaminski, and T. Tiffert, "Quantitative imaging of human red blood cells infected with *Plasmodium falciparum*," *Biophys. J.* **99**, 953–960 (2010).
- ¹⁵Y. M. Serebrennikova, J. Patel, W. K. Milhous, and L. H. García-Rubio, "Quantitative analysis of morphological alterations in *Plasmodium falciparum* infected red blood cells through theoretical interpretation of spectral measurements," *J. Theor. Biol.* **265**, 493–500 (2010).
- ¹⁶P. A. Buffet, I. Safeukui, G. Deplaine, V. Brousse, V. Prendki, M. Thellier, G. D. Turner, and O. M. Puijalón, "The pathogenesis of *Plasmodium falciparum* malaria in humans: Insights from splenic physiology," *Blood* **117**, 381–392 (2011).
- ¹⁷M. Aingaran, R. Zhang, S. K. Law, Z. Peng, A. Undisz, E. Meyer, M. D. Silva, T. A. Burke, T. Spielmann, C. T. Lim, S. Suresh, M. Dao, and M. Marti, "Host cell deformability is linked to transmission in the human malaria parasite *Plasmodium falciparum*," *Cell. Microbiol.* **14**, 983–993 (2012).
- ¹⁸M. Abkarian, M. Faivre, and H. A. Stone, "High-speed microfluidic differential manometer for cellular-scale hydrodynamics," *Proc. Natl. Acad. Sci. U.S.A.* **103**, 538–542 (2006).
- ¹⁹S. S. Lee, Y. Yim, K. H. Ahn, and S. J. Lee, "Extensional flow-based assessment of red blood cell deformability using hyperbolic converging microchannel," *Biomed. Microdevices* **11**, 1021–1027 (2009).
- ²⁰G. Tomaiuolo, M. Barra, V. Preziosi, A. Cassinese, B. Rotoli, and S. Guido, "Microfluidics analysis of red blood cell membrane viscoelasticity," *Lab Chip* **11**, 449–454 (2011).
- ²¹V. Leble, R. Lima, R. Dias, C. Fernandes, T. Ishikawa, Y. Imai, and T. Yamaguchi, "Asymmetry of red blood cell motions in a microchannel with a diverging and converging bifurcation," *Biomicrofluidics* **5**, 044120 (2011).
- ²²S. M. McFaul, B. K. Lin, and H. Ma, "Cell separation based on size and deformability using microfluidic funnel ratchets," *Lab Chip* **12**, 2369–2376 (2012).
- ²³Q. Guo, S. Park, and H. Ma, "Microfluidic micropipette aspiration for measuring the deformability of single cells," *Lab Chip* **12**, 2687–2695 (2012).
- ²⁴D. J. Quinn, I. Pivkin, S. Y. Wong, K.-H. Chiam, M. Dao, G. E. Karniadakis, and S. Suresh, "Combined simulation and experimental study of large deformation of red blood cells in microfluidic systems," *Ann. Biomed. Eng.* **39**, 1041–1050 (2011).
- ²⁵Y. Imai, H. Kondo, T. Ishikawa, C. T. Lim, and T. Yamaguchi, "Modeling of hemodynamics arising from malaria infection," *J. Biomech.* **43**, 1386–1393 (2010).
- ²⁶A. Yeung and E. Evans, "Cortical shell-liquid core model for passive flow of liquid-like spherical cells into micro-pipettes," *Biophys. J.* **56**, 139–149 (1989).
- ²⁷C. T. Lim, E. H. Zhou, and S. T. Quek, "Mechanical models for living cells—a review," *J. Biomech.* **39**, 195–216 (2006).
- ²⁸F. Y. Leong, Q. Li, C. T. Lim, and K. H. Chiam, "Modeling cell entry into a micro-channel," *Biomech. Model. Mechanobiol.* **10**, 755–766 (2011).
- ²⁹J. J. Monaghan, "Smoothed particle hydrodynamics," *Rep. Prog. Phys.* **68**, 1703–1759 (2005).
- ³⁰B. D. Rogers, R. A. Dalrymple, M. Gómez-Gesteira, and A. J. C. Crespo, "User guide for the parallelSPHysics code using MPI v2.0," <http://www.sphysics.org> (2011).
- ³¹M. Gómez-Gesteira, B. D. Rogers, A. J. C. Crespo, R. A. Dalrymple, M. Narayanaswamy, and J. M. Dominguez, "SPHysics—development of a free-surface fluid solver—Part 1: Theory and formulations," *Comput. Geosci.* **48**, 289–299 (2012).
- ³²M. Gómez-Gesteira, A. J. C. Crespo, B. D. Rogers, R. A. Dalrymple, J. M. Dominguez, and A. Barreiro, "SPHysics—development of a free-surface fluid solver—Part 2: Efficiency and test cases," *Comput. Geosci.* **48**, 300–307 (2012).
- ³³U. Seifert, "Configurations of fluid membranes and vesicles," *Adv. Phys.* **46**, 13–137 (1997).
- ³⁴S. Wada and R. Kobayashi, "Numerical simulation of various shape changes of a swollen red blood cell by decrease of its volume," *Trans. Jpn. Soc. Mech. Eng.* **69**, 14–21 (2003).
- ³⁵K. I. Tsubota and S. Wada, "Elastic force of red blood cell membrane during tank-treading motion: Consideration of the membrane's natural state," *Inter. J. Mech. Sci.* **52**, 356–364 (2010).
- ³⁶D. E. Discher, D. H. Boal, and S. K. Boey, "Simulation of the erythrocyte cytoskeleton at large deformation. II. Micropipette aspiration," *Biophys. J.* **75**, 1584–1597 (1998).
- ³⁷T. Omori, T. Ishikawa, D. Barthès-Biesel, A.-V. Salsac, J. Walter, Y. Imai, and T. Yamaguchi, "Comparison between spring network models and continuum constitutive laws: Application to the large deformation of a capsule in shear flow," *Phys. Rev. E* **83**, 041918 (2011).
- ³⁸D. H. Boal and M. Rao, "Topology changes in fluid membranes," *Phys. Rev. A* **46**, 3037–3045 (1992).
- ³⁹R. M. Hochmuth and R. E. Waugh, "Erythrocyte membrane elasticity and viscosity," *Ann. Rev. Physiol.* **49**, 209–219 (1987).
- ⁴⁰C. Dong and R. Skalak, "Leukocyte deformability: Finite element modeling of large viscoelastic deformation," *J. Theor. Biol.* **158**, 173–193 (1992).

- ⁴¹J. J. Monaghan, "Smoothed particle hydrodynamics and its diverse applications," *Ann. Rev. Fluid Mech.* **44**, 323–346 (2012).
- ⁴²E. S. Lee, C. Moulinec, R. Xu, D. Violeau, D. Laurence, and P. Stansby, "Comparisons of weakly compressible and truly incompressible algorithms for the SPH mesh free particle method," *J. Comput. Phys.* **227**, 8417–8436 (2008).
- ⁴³S. M. Hosseini and J. J. Feng, "Pressure boundary conditions for computing incompressible flows with SPH," *J. Comput. Phys.* **230**, 7473–7487 (2011).
- ⁴⁴M. S. Shadloo, A. Zainali, M. Yildiz, and A. Suleman, "A robust weakly compressible SPH method and its comparison with an incompressible SPH," *Int. J. Numer. Methods Eng.* **89**, 939–956 (2012).
- ⁴⁵R. Xu, P. Stansby, and D. Laurence, "Accuracy and stability in incompressible SPH (ISPH) based on the projection method and a new approach," *J. Comput. Phys.* **228**, 6703–6725 (2009).
- ⁴⁶A. Esposito, T. Tiffert, J. M. A. Mauritz, S. Schlachter, L. H. Bannister, C. F. Kaminski, and V. L. Lew, "FRET imaging of hemoglobin concentration in *Plasmodium falciparum*-infected red cells," *PLoS One* **3**, e3780 (2008).
- ⁴⁷Y. K. Park, M. Diez-Silva, G. Popescu, G. Lykotrafitis, W. Choi, M. S. Feld, and S. Suresh, "Refractive index maps and membrane dynamics of human red blood cells parasitized by *Plasmodium falciparum*," *Proc. Natl. Acad. Sci. U.S.A.* **105**, 13730–13735 (2008).
- ⁴⁸H. Shi, A. Li, J. Yin, K. Tan, and C. Lim, "AFM study of the cytoskeletal structures of malaria infected erythrocytes," in *Proceedings of the 13th International Conference on Biomedical Engineering* (2009), Vol. 23, pp. 1965–1968.
- ⁴⁹G. Boedec, M. Leonetti, and M. Jaeger, "3D vesicle dynamics simulations with a linearly triangulated surface," *J. Comput. Phys.* **230**, 1020–1034 (2011).
- ⁵⁰S. M. Hosseini and J. J. Feng, "A particle-based model for the transport of erythrocytes in capillaries," *Chem. Eng. Sci.* **64**, 4488–4497 (2009).
- ⁵¹J. Dupire, M. Socol, and A. Viallat, "Full dynamics of a red blood cell in shear flow," *Proc. Natl. Acad. Sci. U.S.A.* **109**, 20808–20813 (2012).
- ⁵²T. M. Fischer, M. Stohr-Liesen, and H. Schmid-Schonbein, "The red cell as a fluid droplet: Tank tread-like motion of the human erythrocyte membrane in shear flow," *Science* **202**, 894–896 (1978).
- ⁵³Y. Sui, Y. T. Chew, P. Roy, Y. P. Cheng, and H. T. Low, "Dynamic motion of red blood cells in simple shear flow," *Phys. Fluids* **20**, 112106 (2008).
- ⁵⁴R. Skalak, A. Tozeren, R. P. Zarda, and S. Chien, "Strain energy function of red blood cell membranes," *Biophys. J.* **13**, 245–264 (1973).
- ⁵⁵H. Hinghofer-Szalkay and J. E. Greenlea, "Continuous monitoring of blood volume changes in humans," *J. Appl. Physiol.* **63**, 1003–1007 (1987).
- ⁵⁶G. Késmárky, P. Kenyeres, M. Rábai, and K. Tóth, "Plasma viscosity: A forgotten variable," *Clin. Hemorheol. Microcirc.* **39**, 243–246 (2008).
- ⁵⁷G. R. Cokelet and H. J. Meiselman, "Rheological comparison of hemoglobin solutions and erythrocyte suspensions," *Science* **162**, 275–277 (1968).
- ⁵⁸G. Couplier, B. Kaoui, T. Podgorski, and C. Misbah, "Noninertial lateral migration of vesicles in bounded poiseuille flow," *Phys. Fluids* **20**, 111702 (2008).
- ⁵⁹D. A. Fedosov, B. Caswell, and G. E. Karniadakis, "A multiscale red blood cell model with accurate mechanics, rheology, and dynamics," *Biophys. J.* **98**, 2215–2225 (2010).
- ⁶⁰E. Evans, "New membrane concept applied to the analysis of fluid shear- and micropipette-deformed red blood cells," *Biophys. J.* **13**, 941–954 (1973).
- ⁶¹A. G. Maier, B. M. Cooke, A. F. Cowman, and L. Tilley, "Malaria parasite proteins that remodel the host erythrocyte," *Nat. Rev. Microbiol.* **7**, 341–354 (2009).
- ⁶²S. Sanyal, S. Egée, G. Bouyer, S. Perrot, I. Safeukui, E. Bischoff, P. Buffet, K. W. Deitsch, O. Mercereau-Puijalon, P. H. David, T. J. Templeton, and C. Lavazec, "*Plasmodium falciparum* STEVOR proteins impact erythrocyte mechanical properties," *Blood* **119**, e1–e8 (2012).
- ⁶³S. C. Gifford, M. G. Frank, J. Derganc, C. Gabel, R. H. Austin, T. Yoshida, and M. W. Bitensky, "Parallel microchannel-based measurements of individual erythrocyte areas and volumes," *Biophys. J.* **84**, 623–633 (2003).
- ⁶⁴P. Pereira, M.-P. Valignat, J. Bico, and O. Théodoly, "Single cell rheometry with a microfluidic constriction: Quantitative control of friction and fluid leaks between cell and channel walls," *Biomechanics* **7**, 024111 (2013).
- ⁶⁵M. Antia, T. Herricks, and P. K. Rathod, "Microfluidic approaches to malaria pathogenesis," *Cell. Microbiol.* **10**, 1968–1974 (2008).
- ⁶⁶T. Herricks, M. Antia, and P. K. Rathod, "Deformability limits of *Plasmodium falciparum*-infected red blood cells," *Cell. Microbiol.* **11**, 1340–1353 (2009).
- ⁶⁷T. Herricks, K. B. Seydel, M. Molyneux, T. Tayler, and P. K. Rathod, "Estimating physical splenic filtration of *Plasmodium falciparum*-infected red blood cell in malaria patients," *Cell. Microbiol.* **14**, 1880–1891 (2012).
- ⁶⁸L. Tilley, M. W. A. Dixon, and K. Kirk, "The *Plasmodium falciparum*-infected red blood cell," *Int. J. Biochem. Cell Biol.* **43**, 839–842 (2011).
- ⁶⁹B. Schnitzer, T. Sodeman, M. L. Mead, and P. G. Contacos, "Pitting function of the spleen in malaria: Ultrastructural observations," *Science* **177**, 175–177 (1972).